Symmetry-Selected Electron-Energy-Loss Scattering in Diamond

P. E. Batson

IBM Thomas J. Watson Research Center, Yorktown Heights, New York 10598

(Received 18 December 1992)

Inelastic electron scattering using a two-beam channeling condition is used for the first time to create excitations having selectable even or odd symmetry relative to an atom column. The method is first established using plasmon and interband scattering in diamond. Next, for the carbon 1*s* absorption edge, scattering to modes having odd symmetry gives a strong exciton peak. Scattering to modes having even symmetry results in a depressed edge having no exciton peak in evidence.

PACS numbers: 61.14.Rq, 71.35.+z, 78.70.Dm

A core exciton has been observed at the diamond 1*s* absorption edge using photoyield [1] and electron-energy-loss spectroscopies (EELS) [2]. Both methods yielded a binding energy of about 0.2 eV, consistent with a loosely bound Wannier exciton. This was treated within a simple two-band effective mass approximation as described by Elliott [3]. Jackson and Pederson have suggested that this analysis might be inadequate [4]. Their suggestion was based on the apparent similarity between a carbon atom having a charge of $Z+1$ due to the presence of a core hole, and a nitrogen donor, which is known to produce a much larger binding energy, of order 1.7 eV. They pointed out that this picture leads to a qualitatively similar spectrum, because the deep level has an A_1 symmetry, making it inaccessible from the diamond 1*s* core state under dipole selection rules. They therefore deduced that the observed exciton might be a shallow exciton having $2p$ symmetry. Recently, results from x-ray emission spectroscopy suggested that the diamond conduction band edge might be as much as 1 eV higher relative to the 1*s* core level than had been thought previously [5]. This would bring the observed exciton binding energy to 1.2 eV, supporting the Frenkel exciton picture. An arguable difficulty with this view, however, is that it requires some symmetry-breaking mechanism to allow observation of the dipole forbidden exciton having A_1 symmetry.

Thus, there is a need for a reasonably clear determination of the symmetry of the core exciton. This Letter describes EELS experiments which use a channeling geometry to produce an incident swift electron wave function that has selectable even or odd symmetry in the direction of the reciprocal lattice vector associated with the Bragg scattering. Electron channeling has been used in the past to modulate the intensity of the incident electron beam, providing site specific sensitivity for characteristic x-ray production [6] and electron-energy-loss spectroscopy [7]. However, this is the first work that seeks to exploit the symmetry of the electron wave function directly. Recently, inelastic x-ray scattering was demonstrated to be possible using an initial state defined by a standing wave located at the surface [8]. In that experiment, no selection of final-state symmetry was attempted. But it was still possible to access the bulk plasmon energy near the Brillouin zone boundary, and to show that it was split into two bands by interaction with the crystal potential. In the transmission EELS experiment, we can choose the symmetry of the final state by placement of a collection aperture. If sufficient thickness of sample exists below a scattering event, then the scattered wave will be channeled into different directions depending on whether it is symmetric or antisymmetric relative to the atom columns. The crystal defines a grating which, from certain directions, blocks waves except those of a certain symmetry. Thus, if the channeling waves are established within a certain thickness, then both the initial and final states may be controlled to some extent by working in a sample that is about twice that thickness.

These ideas can be developed using two-beam elastic scattering theory, following Hirsch *et al.* [9]. The wave function $\psi(\mathbf{r})$ satisfies Shrödinger's equation for an electron of energy E moving in a periodic potential $V(\mathbf{r}) \equiv \sum_{\mathbf{g}} (U_g/2)\exp(i\mathbf{g}\cdot\mathbf{r})$,

$$\nabla^2\psi(\mathbf{r}) + 2[E - V(\mathbf{r})]\psi(\mathbf{r}) = 0 , \tag{1}$$

where I use atomic units. I consider here only one Fourier component of the crystal periodic potential, $\mathbf{g} \equiv \mathbf{g}_{220}$, the first allowed Bragg reflection in the [001] oriented diamond crystal. This choice favors solutions that do not differentiate between the two carbon positions in the primitive unit cell. The general solution for ψ becomes

$$\psi^j(\mathbf{r}) = C_0^j e^{i\mathbf{k}^j\cdot\mathbf{r}} + C_g^j e^{i(\mathbf{k}^j+\mathbf{g})\cdot\mathbf{r}} , \tag{2}$$

where the coefficients, C_g^j are obtained from the system of linear equations formed by substitution of ψ into Eq. (1). The superscript j refers to the two allowed values of $\mathbf{k}$ for the electron in the crystal given by the solutions for the dispersion relation,

$$(k^2 - K^2)[(\mathbf{k}+\mathbf{g})^2 - K^2] - U_g U_{-g} = 0 , \tag{3}$$

and K is the magnitude of the swift electron wave vector in the crystal corrected for the crystal average inner potential, U_0.

The wave function appropriate for a depth z into the crystal is a linear combination of the two solutions in Eq. (2), chosen to satisfy boundary conditions at the top of the crystal. In the two-beam case, this is a function of the depth z and the horizontal distance x, parallel to $\mathbf{g}_{220}$. After some algebra, this becomes

$$\psi = e^{i\mathbf{K}\cdot\mathbf{r}} e^{isz/2}\{\cos(\tfrac{1}{2}\Delta kz) - i\sin(\tfrac{1}{2}\Delta kz)[\cos\beta - \sin\beta e^{igx}]\}, \quad (4a)$$

$$s \approx g\tan\Delta\theta, \quad \cot\beta = \frac{s\xi}{2\pi}, \quad \Delta k = (s^2 + 4\pi^2/\xi^2)^{1/2}, \quad (4b)$$

where s defines the distance from the Ewald sphere to the reciprocal lattice point g, for a deviation $\Delta\theta$ from the exact Bragg condition θ. $\xi \approx K\cos\theta/2\pi U_g$ is the extinction thickness for the Bragg reflection employed for the channeling. β is defined in the upper half plane, so that $s > 0$ implies $\beta < \pi/2$, and $s < 0$ implies $\beta > \pi/2$. Thus, $\cos\beta$ changes sign with s, causing a change in symmetry in the x direction with deviation from the exact Bragg condition. This effect is maximized at the depth, $z = \pi/\Delta k$, where the first term in Eq. (4a) is zero. At this depth, we may write in simplified form for $s = \pm 2\pi/\xi$:

$$\psi_s^0 = e^{i\mathbf{K}\cdot\mathbf{r}} e^{i\pi/2\sqrt{2}} \sqrt{2} e^{igx/2}[-\sin(gx/2)],$$
$$\psi_{-s}^0 = e^{i\mathbf{K}\cdot\mathbf{r}} e^{-i\pi/2\sqrt{2}} \sqrt{2} e^{igx/2}[i\cos(gx/2)]. \quad (5a)$$

There is also a second set of solutions for an incoming beam positioned near the opposite Bragg reflecting position:

$$\psi_s^g = e^{i(\mathbf{K}+\mathbf{g})\cdot\mathbf{r}} e^{i\pi/2\sqrt{2}} \sqrt{2} e^{-igx/2}[\sin(gx/2)],$$
$$\psi_{-s}^g = e^{i(\mathbf{K}+\mathbf{g})\cdot\mathbf{r}} e^{-i\pi/2\sqrt{2}} \sqrt{2} e^{-igx/2}[i\cos(gx/2)]. \quad (5b)$$

This set is identical to the set (5a) except for a phase shift of π radians in the solution for $+s$. These solutions also describe the behavior of a scattered wave, propagating from the position of the inelastic scattering event to the bottom of the crystal. Figure 1 shows dispersion surfaces and direction of wave propagation for the swift electron within the crystal defined above in Eq. (3) following the construction given by Howie [10]. The k_z direction is grossly foreshortened for clarity. The upper dispersion curves give solutions for electrons moving at the primary energy E. The lower set gives solutions for the energy-loss electrons. Each set consists of a higher-energy, symmetric branch and a lower-energy, antisymmetric branch. The points labeled $\psi_{\pm s}^{0,g}$ summarize the positions of the solutions used in this experiment. I summarize by ellipses the positions and sizes (relative to $\mathbf{g}_{220}$) of collimation and collection apertures to require the transitions (a) and (b). In this construction, I have labeled the wave functions relative to the $\mathbf{g}_{220}$ direction, rather than relative to the incident beam direction. This allows the final-state labeling to remain constant, and simplifies the diagram. An alternative construction using $\mathbf{g}_{220}$ and $-\mathbf{g}_{220}$ would require two illustrations.

Having now defined a set of initial and final swift electron states which are not simple plane waves, it is useful to redefine the matrix element for scattering. Following the notation of Pines and Nozières [11], the matrix element can be written,

$$M = \sum_i \langle\psi_f(\mathbf{r})|\langle\phi_n(\mathbf{r}_i)|\mathcal{V}(\mathbf{r}_i - \mathbf{r})|\phi_0(\mathbf{r}_j)\rangle|\psi_0(\mathbf{r})\rangle, \quad (6a)$$

where $\mathcal{V}$ is the Coulomb potential, $\psi_{f,0}$ denotes the swift

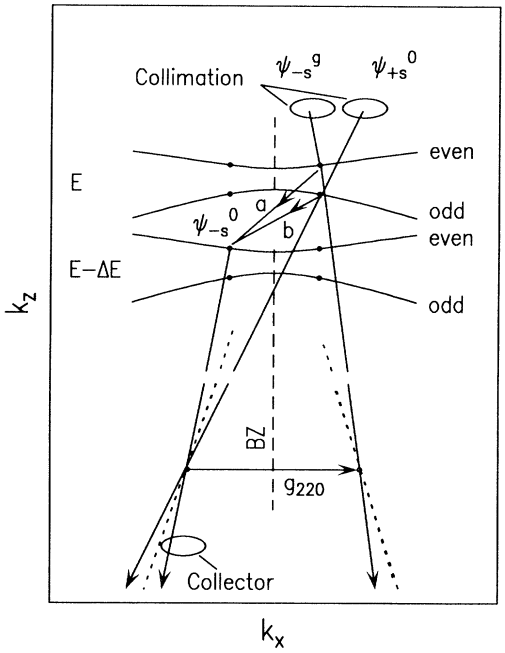

FIG. 1. Dispersion surfaces and direction of propagation near the $\mathbf{g}_{220}$ Brillouin zone boundary for swift electrons within the sample. Two sets of surfaces summarize behavior for electrons at the incident energy E and after energy loss ΔE. Swift electron transitions used in this work are indicated (a and b). Schematic positions for initial collimation and final-state collection apertures are shown. The dispersion branches are labeled for even and odd symmetry. The Brillouin zone boundary is indicated (BZ).

electron wave function and $\phi_{n,0}$ denotes the specimen excitations, and the sum is over specimen electrons. We may Fourier analyze $\mathcal{V}$ and express the matrix element as a sum over plane-wave expansions of the specimen states,

$$M = \sum_q V_q \langle\psi_f(\mathbf{r})|\sum_i \langle\phi_n(\mathbf{r}_i)|e^{-i\mathbf{q}\cdot\mathbf{r}_i}|\phi_0(\mathbf{r}_i)\rangle e^{i\mathbf{q}\cdot\mathbf{r}}|\phi_0(\mathbf{r})\rangle,$$
$$= \sum_{q>0} V_q \langle\psi_f(\mathbf{r})|\rho_{-q}e^{-i\mathbf{q}\cdot\mathbf{r}} + \rho_q e^{i\mathbf{q}\cdot\mathbf{r}}|\psi_0(\mathbf{r})\rangle, \quad (6b)$$

where $\rho_q \equiv (\rho_{\mathbf{q}}^{\dagger})^{n0}$ is the matrix element of a charge density fluctuation taken between the ground state and the nth excited state of the specimen. I have also used the fact that V_q, the Fourier transform of $\mathcal{V}(r)$, is an even function of q.

Expression (6b) is written to highlight the symmetry of both the probe and specimen transitions. If the specimen excitation is invariant under translation, for instance high-energy single-particle transitions and plasmons, then ρ_q is of order q^2. If the excitation is not invariant under translation, for instance interband transitions, then ρ_q is of order q. Thus, the quantity within the matrix element of expression (6b) will have even parity for plasmons, and odd parity for interband transitions [12]. It is important to realize that expression (6b) contains many "off-diagonal" terms of the dielectric response, summed co-

herently to produce the matrix element. We may now ascertain whether the matrix element for scattering is finite by inspection of expression (6b), given the known parities of the specimen transition and the swift electron initial and final states.

The instrument used here was the VG Microscopes, HB501 scanning transmission electron microscope, operated in this case at 120 keV. The electron spectrometer is a Wien filter using deceleration to obtain 0.2 eV resolution [13]. The $1s$ core spectra were sharpened by deconvolution [14] to a 0.32 eV resolution, limited by the statistical accuracy of the data. This work was made possible by a recent improvement of the system to include a charge-coupled-device array detector. This produced an increase in detection sensitivity of $\times 100$ over the photodiode array as described in Ref. [13] below. The diamond was wedge shaped with a [100] axis parallel to the beam direction. Electron optical conditions were chosen to produce a roughly 2–5 nm spot size using two apertures to define an illumination and collection range of about 0.5 Å^{-1} centered about 0.5 Å^{-1} away from exact [220] two-beam diffraction conditions ($\mathbf{g}_{220} \approx 5$ Å^{-1}) near the optimum position of 0.34 Å^{-1} for $s = 2\pi/\xi$ with $\xi \approx 690$ Å using 120 keV electrons ($K \approx 186$ Å^{-1}). Analyses were then performed in areas having thicknesses in the $(0.75\text{–}1.25)\xi$ range using the various initial- and final-state wave functions defined in Eqs. (5) above. All of the results reported here used a collection aperture centered inside the [220] diffraction condition and I define this wave function as $\psi_f \equiv \psi^0_{-s}$, as shown in Fig. 1.

Results for the low-energy-loss region of diamond are shown in Fig. 2. I show three results: (a) even parity scattering using $\psi_i \equiv \psi^g_{-s}$, (b) odd parity scattering using $\psi_i \equiv \psi^0_{+s}$, and (c) axial, small angle scattering, using $\psi_i \equiv \psi^0_{-s}$. I have normalized these results so that the scattering peaks at 0 eV energy loss are normalized. In cases (a) and (b), these are due to quasielastic phonon scattering. In case (c) the peak is due to swift electrons which have not been inelastically scattered.

We can see immediately that the plasmon scattering near 34 eV is depressed on going from even parity, case (a), to odd parity, case (b). As we noted above, this is expected due to the even character of the charge-density fluctuations for plasmon behavior as noted above. Case (c) is largely due to small angle scattering, because the initial and final swift electron directions overlap. Thus long-wavelength even and odd parity scattering in the y or z direction dominates the results. This is the normally obtained result for coaxial beam definition and collection apertures. I compare this result with $\text{Im}(-1/\varepsilon)$ calculated using the known optical constants for diamond [15], extrapolated to high energy using a simple free electron dielectric constant,

$$\varepsilon_{\text{free}}(\omega) = 1 - \omega_p^2/(\omega + i\gamma)^2 , \tag{7}$$

where $\omega_p = 33$ eV is a plasma frequency and $\gamma = 8.4$ eV is a damping parameter. These values are qualitatively correct, but detailed comparisons with previous measurements should take into account the model represented by Eq. (7). The results reproduce both plasmon and interband scattering as expected.

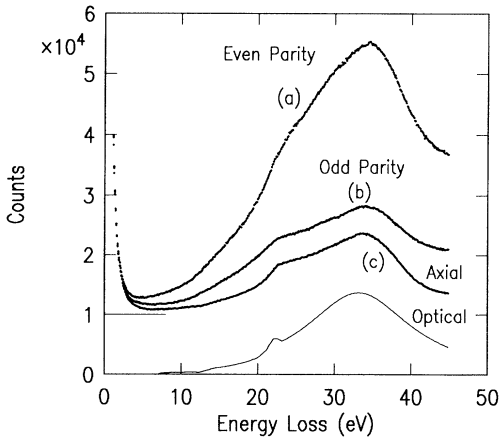

FIG. 2. Low-loss scattering for even parity (a), odd parity (b), and axial collection (c). The spectra have been normalized at zero energy. Case (c) has been compared with the prediction using the known optical constants extrapolated to high energy.

In order for expression (6b) to fully control the observed scattering, all collected intensity must be the result of single inelastic scattering events. But the scattering in cases (a) and (b) above also includes multiple events of the type phonon plus plasmon. These have been treated for the case of aluminum, and it was found that the multiple scattering may be adequately approximated by the properly scaled angle integrated energy-loss spectrum [16]. Case (c) approximates this result. A simple subtraction of case (c) from cases (a) and (b) then should produce the parity-selected spectral results.

These are shown in Fig. 3. We see that the even parity result is completely smooth in the 5–30 eV range. All direct interband scattering has been suppressed by the enforced even character of the swift electron transition. On the other hand, in the odd parity result the plasmon is almost completely suppressed, and structure in the 5–25 eV range is enhanced. We can understand the odd parity structure better by eliminating the plasmon polarizability form ε:

$$\varepsilon_{\text{odd}} = \varepsilon_{\text{optical}} - \text{Re}(\varepsilon_{\text{free}} - 1) . \tag{8}$$

Thus, the odd parity result is compared with $\text{Im}(-1/\varepsilon_{\text{odd}})$. The agreement is striking. The quantity in Eq. (8) and the results in Fig. 3 represent a new response function for solid-state matter.

The low-energy-loss results are therefore explainable in terms of symmetry selection. We could use the terms dipole and nondipole in place of odd and even, but one difference remains. Normally we think of dipole interactions in terms of long-wavelength optical absorption or scattering. The wavelength of the specimen fluctuations in these experiments is of the order of the crystal unit cell size. However, fluctuations having longer wavelength will be accessible according to their symmetry.

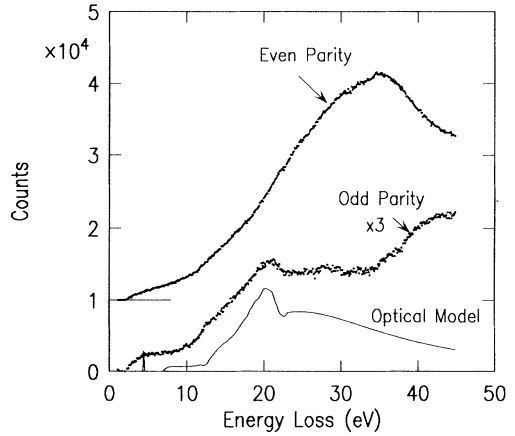

FIG. 3. Low-loss regions after subtraction of multiple phonon plus plasmon scattering. The even parity results show only plasmon scattering. The odd parity results are compared with the odd parity part of the scattering from the optical constants.

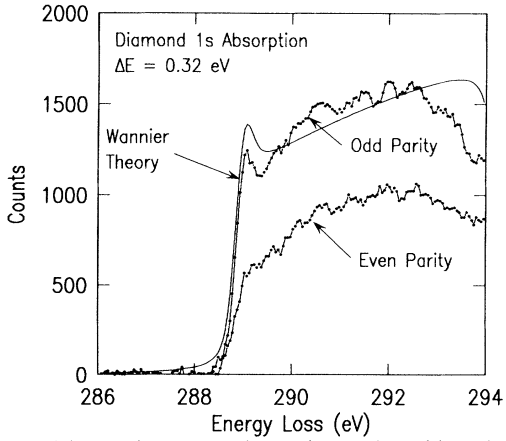

FIG. 4. Diamond 1*s* core absorption. The odd parity result shows a strong core exciton. The even parity result shows a depressed edge exhibiting no core exciton.

Having now established that symmetry selection is possible in this experiment, I now describe the carbon 1*s* core absorption, using the scattering conditions of cases (a) and (b) above. These are summarized in Fig. 4. In this case, the core scattering extends with high probability to fairly large angles, so that no multiple scattering correction is necessary. We see that the odd parity scattering shows a strong exciton. In addition, the exciton energy appears to be coincident with the x-ray photoyield results. This supports the recent suggestion that the swift electron plasmon wake influences the measured energy of the diamond core exciton [2]. In this case, the odd parity scattering suppresses the plasmon wake, preventing it from influencing the exciton binding energy. The even parity result shows a suppressed absorption, as expected. That the suppression is not complete is probably due to the very relaxed channeling conditions limited by the finite collimation and collection apertures. The core exciton is absent in this result.

If the exciton were 1*s*-like, as has been suggested recently, it should be enhanced in the even parity scattering case. If the exciton has a dipole allowed 2*p* symmetry, as has also been suggested, then we should expect to see a strong 1*s* exciton, nearly 1.5 eV below the absorption onset, in the even parity result. This does not occur.

Thus, it appears that the weakly bound Wannier picture is a better description of the diamond core exciton than the nitrogen donor model. This is not precluded by symmetry-selection rules as long as the crystal basis set, used to construct the Wannier exciton, includes *p*-like orbitals. These are plentiful near the diamond conduction band edge. The observations reported here are the first to take advantage of the channeling symmetry of both the initial and final swift electron states. Therefore, there are still many details to explain and alternative scattering geometries to explore. In particular, this experiment utilized the crystal to define the lateral spatial dependence of the swift electron wave function. In the future, new instruments will be able to directly position an ultrafine probe near or on a heterogeneous object. Then the arguments here may be useful for understanding the scattering. In particular, more general formulations of the scattering matrix elements, such as given in Eq. (6b) above, will become useful. It is hoped that this work will interest others in beginning careful experiments along these lines.

[1] J. F. Morar, F. J. Himpsel, G. Hollinger, G. Hughes, and J. L. Jordan, Phys. Rev. Lett. **54**, 1960 (1985).
[2] P. E. Batson and J. Bruley, Phys. Rev. Lett. **67**, 350 (1991), P. E. Batson, Phys. Rev. B (to be published).
[3] R. J. Elliott, Phys. Rev. **108**, 1384 (1957).
[4] K. A. Jackson and M. R. Pederson, Phys. Rev. Lett. **67**, 2521 (1991).
[5] J. Nithianandam, Phys. Rev. Lett. **69**, 3108 (1992).
[6] D. Cherns, A. Howie, and M. H. Jacobs, Z. Naturforsch. **28A**, 565 (1973).
[7] J. Tafto and O. L. Krivanek, Phys. Rev. Lett. **48**, 560 (1982).
[8] W. Schulke and A. Kaprolat, Phys. Rev. Lett. **67**, 879 (1991).
[9] P. B. Hirsch, A. Howie, R. B. Nicholson, D. W. Pashley, and M. J. Whelan, *Electron Microscopy of Thin Crystals* (Butterworths, London, 1965), Chap. 9.
[10] A. Howie, Proc. R. Soc. London A **271**, 268 (1963).
[11] D. Pines and P. Nozières, *Theory of Quantum Liquids* (Benjamin, New York, 1966), pp. 85–87.
[12] *Theory of Quantum Liquids* (Ref. [11]), p. 221.
[13] P. E. Batson, Rev. Sci. Instrum. **57**, 43 (1986); **59**, 1132 (1988).
[14] P. E. Batson, D. W. Johnson, and J. C. H. Spence, Ultramicroscopy **41**, 137 (1992).
[15] H. R. Philipp and E. A. Taft, Phys. Rev. **136**, A1445 (1964).
[16] P. E. Batson and J. Silcox, Phys. Rev. B **27**, 5224 (1983).